

# Tuning Nonradiative Recombination via Cation Substitution in Inorganic Antiperovskite Nitrides

Sanchi Monga\* and Saswata Bhattacharya†

Department of Physics, Indian Institute of Technology Delhi, New Delhi 110016, India

Inorganic antiperovskite nitrides have recently emerged as promising materials for photovoltaic applications, yet their nonradiative recombination dynamics remain largely unexplored. Here, we examine the influence of X-site cation substitution on the nonradiative electron-hole recombination in  $X_3\text{NSb}$  ( $X = \text{Ca}, \text{Sr}, \text{and Ba}$ ). Ca- and Sr-based compounds adopt a cubic phase, whereas Ba stabilizes in a hexagonal structure, introducing pronounced symmetry-driven effects. Substituting Ca with Sr narrows the band gap, suppresses octahedral and band-edge fluctuations, reduces nonadiabatic (NA) coupling by  $\sim 54\%$ , and extends carrier lifetimes by a factor of 2.5. In contrast, Ba substitution increases lattice distortion, widens the band gap, enhances NA coupling, beyond that of  $\text{Sr}_3\text{NSb}$ , and accelerates recombination through stronger lattice fluctuations. The resulting band gap fluctuations in  $\text{Ba}_3\text{NSb}$  also shorten decoherence times, following the trend  $\text{Ba}_3\text{NSb} < \text{Ca}_3\text{NSb} < \text{Sr}_3\text{NSb}$ . Our results demonstrate how the interplay between band gap, NA coupling, and decoherence time governs recombination lifetimes, with  $\text{Sr}_3\text{NSb}$  exhibiting the longest lifetime. These findings highlight the coupled influence of cation chemistry and crystal symmetry in tailoring carrier dynamics for high-performance antiperovskite-based optoelectronics materials.

## I. INTRODUCTION

Organic-inorganic lead halide perovskites (LHPs), such as  $\text{CH}_3\text{NH}_3\text{PbI}_3$  ( $\text{MAPbI}_3$ ), have garnered significant attention for solar light harvesting applications due to their remarkable properties, including a suitable band gap, strong optical absorption, long carrier diffusion lengths, and extended carrier lifetimes [1–4]. These attributes have driven a rapid increase in photo-conversion efficiency (PCE), rising from 3.8% to over 26% in recent years [5]. Despite this progress, the commercial viability of LHPs remains hindered by their environmental instability [6, 7], necessitating the search for alternative compositions that enhance stability while preserving or surpassing their desirable optoelectronic properties.

Antiperovskites, which originate from an electronic inversion of the perovskite structure, have recently emerged as promising candidates for photovoltaic applications [8–16]. Their general structural formula is  $X_3\text{BA}$ , where A and B are different sized anions, and X is a cation. This inversion of ions results in distinct electronic properties in comparison to LHPs while simultaneously expanding the compositional space for exploration. In our previous work [17], we conducted a comprehensive first-principles investigation of a class of antiperovskite nitrides,  $X_3\text{BA}$  (where  $X = \text{Mg}, \text{Ca}, \text{Sr}, \text{Ba}$ ,  $B = \text{N}$ , and  $A = \text{As}, \text{Sb}$ ), focusing on their electronic, optical, excitonic, and polaronic properties. Our findings revealed that Sb-based antiperovskite nitrides exhibit optimal band gaps, low effective masses of charge carriers, small exciton binding energies, weak electron-phonon coupling, and high carrier mobilities—exceeding those of  $\text{MAPbI}_3$ . These characteristics underscore their potential for solar light

harvesting applications.

The performance of solar cells is critically governed by the dynamics of photoexcited charge carriers. Nonradiative recombination processes dissipate carrier energy as heat, thereby constraining PCE. Therefore, suppressing nonradiative recombination is essential for enhancing photovoltaic performance. In recent years, the development and application of *ab initio* nonadiabatic molecular dynamics (NAMD) approaches have substantially advanced the understanding of charge carrier lifetimes in LHPs. Significant efforts to mitigate nonradiative losses in LHPs have focused on strategies such as surface passivation, compositional engineering, and dimensionality control [18–22]. First-principles NAMD simulations have further elucidated the influence of structural and chemical features—including grain boundaries, dopants, and environmental effects such as moisture exposure—on charge carrier lifetimes [23–28]. These studies collectively demonstrate that nonradiative pathways can be strategically suppressed by tailoring intrinsic and extrinsic material properties, with several computational predictions corroborated experimentally [18, 19, 29, 30]. Despite these advances in LHPs, the excited-state dynamics of antiperovskites remain largely unexplored. Given their promising electronic and optical characteristics, a comprehensive understanding of their nonradiative recombination mechanisms is essential to assess their potential for photovoltaic applications.

In this work, we investigate the nonradiative recombination dynamics of  $X_3\text{NSb}$  ( $X = \text{Ca}, \text{Sr}, \text{Ba}$ ) antiperovskite nitrides using real-time time-dependent density functional theory (TDDFT) [31] combined with NAMD. We focus on two central aspects: (i) the influence of increasing the X-site cation size (Ca to Sr to Ba) and (ii) the role of crystal symmetry, with  $\text{Ca}_3\text{NSb}$  and  $\text{Sr}_3\text{NSb}$  adopting cubic  $Pm\bar{3}m$  symmetry and  $\text{Ba}_3\text{NSb}$  stabilizing in a distorted hexagonal  $P6_3/mmc$  phase. Our analysis reveals that variations in cation chemistry and structural

\* sanchi@physics.iitd.ac.in [SM]

† saswata@physics.iitd.ac.in [SB]

symmetry govern the band gap, lattice dynamics, and electronic couplings in distinct ways, collectively shaping carrier recombination behavior. These findings highlight the critical role of structural–electronic interplay in guiding the rational design of antiperovskite materials with improved excited-state lifetimes for optoelectronic applications.

## II. COMPUTATIONAL DETAILS

We perform *ab initio* NAMD simulations using the decoherence-induced surface hopping (DISH) method [32, 33], within the classical path approximation, as implemented in the PYXAID package [34, 35]. In this framework, the nuclear motion—associated with heavier and slower atoms—is treated semiclassically, whereas the electronic degrees of freedom are described quantum mechanically using TDDFT [31]. Decoherence, arising from elastic electron–phonon scattering that disrupts superpositions between electronic states, plays a critical role in regulating quantum transitions. Since decoherence typically occurs on timescales shorter than those of interband transitions, its inclusion is essential for accurately capturing nonradiative electron–hole recombination processes. In the DISH algorithm, quantum transitions emerge as a consequence of decoherence, which provides the physical basis for surface hops. Decoherence time is estimated as the pure-dephasing time, evaluated via the second-order cumulant approximation of optical response theory [36].

First-principles density functional theory (DFT) calculations [37, 38] are performed using the Vienna *ab initio* Simulation Package (VASP) [39, 40]. The projector augmented-wave (PAW) method [41] is employed to accurately describe the interactions between valence electrons and the ionic cores. Structural optimization is carried out using the generalized gradient approximation (GGA) with the Perdew–Burke–Ernzerhof (PBE) exchange–correlation functional [42]. A  $\Gamma$ -centered  $\mathbf{k}$ -point mesh of  $6 \times 6 \times 6$  and a plane-wave cutoff energy of 550 eV are used to ensure convergence. The atomic positions are relaxed until the Hellmann–Feynman forces on each atom are less than  $10^{-3}$  eV/Å. The calculated lattice parameters are listed in Table 1 of the Supporting Information (SI) and they show good agreement with previously reported values [16, 43]. For electronic structure calculations, the hybrid Heyd–Scuseria–Ernzerhof (HSE06) functional [44] is employed, including the spin–orbit coupling (SOC).

*Ab initio* molecular dynamics (AIMD) simulations are carried out using the Quantum Espresso (QE) package [45]. Supercells of dimension  $2 \times 2 \times 2$  for  $\text{Ca}_3\text{NSb}$  and  $\text{Sr}_3\text{NSb}$ , and  $2 \times 2 \times 1$  for  $\text{Ba}_3\text{NSb}$  are constructed. Following geometry optimization, these supercells are heated to 300 K for a total simulation time of 13 ps with a time step of 1 fs, employing the Verlet algorithm within the canonical (NVT) ensemble. The initial 8 ps of each trajectory is considered for thermal equilibration, and the subsequent

5 ps is used for the generation of the nonadiabatic (NA) Hamiltonian. All NAMD simulations are performed at the  $\Gamma$ -point using the PBE exchange–correlation functional. The use of a single  $\mathbf{k}$ -point is justified by the direct band gap nature of these antiperovskite nitrides, with both the valence band maximum (VBM) and conduction band minimum (CBM) located at the  $\Gamma$ -point (see Fig. 1 of SI). To extend the observation window for recombination dynamics, the NA Hamiltonian extracted from this 5 ps segment is iterated multiple times. The first 50 geometries are chosen as initial configurations, and for each geometry, 10,000 stochastic realizations are performed to ensure convergence. SOC effects are excluded from the NAMD simulations, as they do not significantly alter the band gap magnitude (see Table 2 of SI), while introducing a substantial increase in computational cost.

The GGA-PBE functional is known to underestimate band gaps. Our previous work [17] demonstrates that, for  $\text{Sr}_3\text{NSb}$ , the quasiparticle  $G_0W_0$  approximation on top of HSE06+SOC ( $G_0W_0@HSE06+SOC$ ) yields band gaps in excellent agreement with experiment. However, using hybrid functionals or beyond in NAMD simulations is computationally prohibitive. Therefore, for the present study, we employ the PBE functional, which offers a reasonable balance between computational cost and accuracy, and is widely used for both inorganic and organic perovskites [22, 46, 47]. In order to correct for the band gap underestimation in PBE-based NAMD simulations, a scissor operator is applied. The magnitude of the correction corresponds to the difference between the  $G_0W_0@HSE06+SOC$  and time averaged PBE band gaps, thereby enabling a more realistic estimation of recombination lifetimes. It is important to note that the objective here is to obtain a qualitative understanding of lifetime trends rather than absolute quantitative accuracy. The time-averaged band gaps, obtained by averaging the instantaneous band gaps over a 5 ps MD trajectory, along with the band gaps computed using hybrid HSE06 functional, and the  $G_0W_0$  approximation, are reported in Table 2 of SI.

## III. RESULTS

### A. Geometric structure

Fig. 1 (a) and (b) show the unit cells of  $\text{X}_3\text{NSb}$  ( $\text{X} = \text{Ca}, \text{Sr}, \text{and Ba}$ ) antiperovskite nitrides.  $\text{Ca}_3\text{NSb}$  and  $\text{Sr}_3\text{NSb}$  crystallize in the cubic  $Pm\bar{3}m$  structure, whereas  $\text{Ba}_3\text{NSb}$  adopts a distorted hexagonal  $P6_3/mmc$  phase as its ground state. In the ideal cubic structure (Fig. 1 (a)), Sb atoms occupy the cuboctahedral center surrounded by eight  $\text{NX}_6$  octahedra located at the corners of the cube. Substituting the X-site cation from Ca to Sr to Ba leads to a systematic increase in the intra-octahedral X–N bond lengths, thereby enlarging the  $\text{NX}_6$  octahedra and lattice parameters (see Table 1 of SI). The average

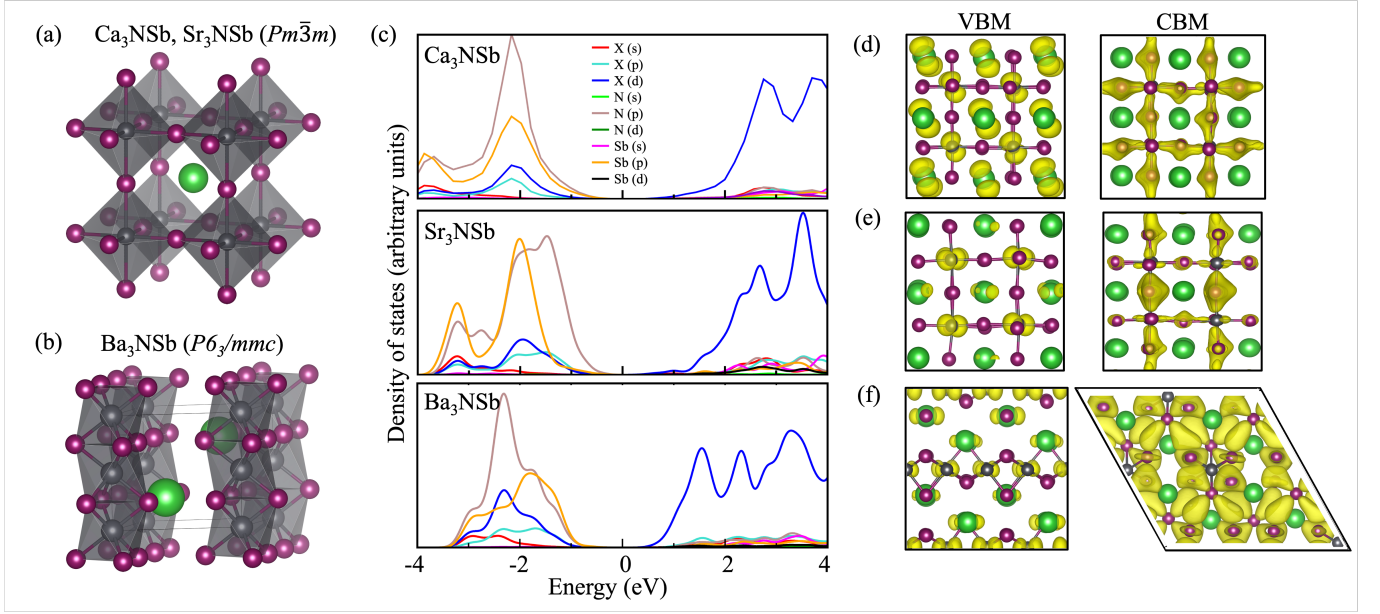


FIG. 1. Unit cells of (a)  $\text{Ca}_3\text{NSb}$  and  $\text{Sr}_3\text{NSb}$ , (b)  $\text{Ba}_3\text{NSb}$ . (c) Atom- and orbital-resolved density of states for the investigated antiperovskites. (d-f) Spatial charge distributions corresponding to the valence band maximum (VBM) and conduction band minimum (CBM) for  $\text{Ca}_3\text{NSb}$ ,  $\text{Sr}_3\text{NSb}$ , and  $\text{Ba}_3\text{NSb}$ , respectively. Grey, purple, and green spheres represent nitrogen, X-site cations, and antimony atoms, respectively.

X–N bond lengths increase from 2.437 Å ( $\text{Ca}_3\text{NSb}$ ) to 2.598 Å ( $\text{Sr}_3\text{NSb}$ ) and 2.686 Å ( $\text{Ba}_3\text{NSb}$ ). In  $\text{Ba}_3\text{NSb}$ , the larger ionic radius of Ba enhances repulsion between Ba and N atoms, thereby, destabilizing the cubic symmetry and favoring a hexagonal configuration.

### B. Static electronic properties

Figure 1 (c-f) depicts the atom- and orbital-resolved density of states (DOS) near the band edges, along with the spatial charge distributions associated with the VBM and CBM. Among all  $\text{X}_3\text{NSb}$  compounds, the VBM is dominated by N and Sb  $p$  orbitals, while the CBM primarily arises from the  $d$  orbitals of the X-site cations. Unlike conventional LHPs, where A-site cations make negligible contributions to the frontier electronic states, the A-site atoms in  $\text{X}_3\text{NSb}$  antiperovskites (A=Sb) contribute significantly to the band edges, highlighting the active role of all atomic constituents. Substituting Ca with Sr reduces Sb  $5p$ –N  $2p$  hybridization, likely due to the increased Sb–N distances in  $\text{Sr}_3\text{NSb}$ . In both Ca and Sr compounds, Sb  $5p$  states lie lower in energy than N  $2p$  states. In contrast,  $\text{Ba}_3\text{NSb}$  exhibits a qualitatively distinct behavior, wherein the Sb  $5p$  levels reside above the N  $2p$  states, and exhibit strong hybridization at the VBM. Remarkably, this enhanced hybridization persists despite the monotonic increase in Sb–N distances from  $\text{Ca}_3\text{NSb}$  (4.224 Å) to  $\text{Sr}_3\text{NSb}$  (4.554 Å) to  $\text{Ba}_3\text{NSb}$  (4.644 Å). This indicates that the incorporation of Ba, accompanied by reduced symmetry and lattice distortions in

the hexagonal  $\text{Ba}_3\text{NSb}$  phase, modifies the local bonding environment, shifts the  $p$ -orbital energy alignments, and facilitates stronger Sb–N hybridization despite longer Sb–N bond distances.

The electronic band structures calculated using the HSE06 hybrid functional with SOC are presented in Fig. S1 of SI. All compounds exhibit direct band gaps at the  $\Gamma$ -point, with values of 1.02 eV, 0.87 eV, and 1.18 eV for  $\text{Ca}_3\text{NSb}$ ,  $\text{Sr}_3\text{NSb}$ , and  $\text{Ba}_3\text{NSb}$ , respectively. Among the cubic phases (Ca and Sr analogs), the band gap decreases from Ca to Sr, consistent with the findings of Mochizuki *et al.* [11], who reported a positive correlation between the band gap and the inverse lattice constant in cubic inorganic antiperovskite nitrides. This trend originates from the lowering of the X  $d$  orbital energies with increasing ionic radius, which reduces the CBM energy and narrows the band gap [12]. In contrast,  $\text{Ba}_3\text{NSb}$  exhibits a larger band gap due to structural distortions that stabilize a hexagonal ground-state phase instead of the cubic symmetry retained by its Ca and Sr counterparts [16]. Such distortion-driven band gap widening is also well documented in conventional perovskites [48–50], and is clearly manifested in the case of  $\text{Ba}_3\text{NSb}$ . Thus, both the X-site cation size and the crystal’s structural symmetry play an important role in tuning the electronic properties of  $\text{X}_3\text{NSb}$  antiperovskites.

TABLE I. Root mean square fluctuation (RMSF) of the atomic positions for the X-site ion, N, and Sb atoms in Å for  $\text{Ca}_3\text{NSb}$ ,  $\text{Sr}_3\text{NSb}$ , and  $\text{Ba}_3\text{NSb}$ .

$\text{X}_3\text{NSb}$	X	N	Sb
$\text{Ca}_3\text{NSb}$	0.085	0.087	0.065
$\text{Sr}_3\text{NSb}$	0.068	0.097	0.067
$\text{Ba}_3\text{NSb}$	0.058	0.101	0.061

### C. Dynamical structural and electronic properties

AIMD simulations provide valuable insights into the time-dependent structural behavior of these compounds. Upon thermal excitation to 300 K, atomic fluctuations arise that influence both electron-hole and electron-phonon interactions. To quantify these fluctuations, we compute the root mean square fluctuation (RMSF) of each atomic species over a 5 ps trajectory (Table I). For the X-site cations, RMSF values decrease systematically from Ca to Sr to Ba, due to increasing atomic mass of the X-site cation, which suppresses thermal motion. Nitrogen atoms, however, display progressively larger RMSF values in  $\text{Sr}_3\text{NSb}$  and  $\text{Ba}_3\text{NSb}$  compared with  $\text{Ca}_3\text{NSb}$ , increasing monotonically with the X-site ionic radius. This behavior can be attributed to the elongation of X–N bonds and the associated increase in lattice free volume, which allows greater spatial freedom for N displacements. The RMSF of Sb changes minimally between  $\text{Ca}_3\text{NSb}$  and  $\text{Sr}_3\text{NSb}$ , with minor variations likely originating from long-range lattice effects. In  $\text{Ba}_3\text{NSb}$ , the slightly lower RMSF value may be attributed to symmetry breaking or stiffer local bonding.

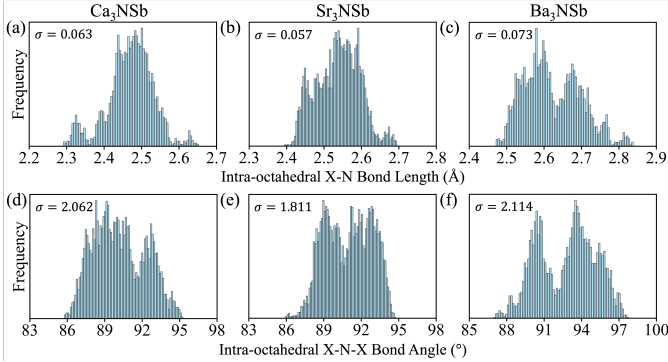


FIG. 2. Statistical distribution of (a-c) intra-octahedral X-N bond lengths and (d-f) intra-octahedral X-N-X bond angles, computed using AIMD simulations, for  $\text{Ca}_3\text{NSb}$ ,  $\text{Sr}_3\text{NSb}$ , and  $\text{Ba}_3\text{NSb}$ . Standard deviations ( $\sigma$ ) of the bond length and bond angle fluctuations are listed.

Thermal excitation also induces a noticeable expansion in the intra-octahedral X-N bond lengths, with time-averaged values of 2.449 Å, 2.626 Å, and 2.687 Å for  $\text{Ca}_3\text{NSb}$ ,  $\text{Sr}_3\text{NSb}$ , and  $\text{Ba}_3\text{NSb}$ , respectively. These values are obtained by averaging all intra-octahedral X-N bond lengths over the entire 5 ps AIMD trajectory.

To quantify the variability of these bond lengths, we construct histograms of the X-N distances, depicted in Fig. 2 (a-c). The associated standard deviations ( $\sigma$ ) reveal that  $\text{Ba}_3\text{NSb}$  exhibits the widest distribution, indicating substantial thermal fluctuations, whereas  $\text{Sr}_3\text{NSb}$  displays the narrowest, reflecting a higher degree of structural rigidity. Similar trends are observed in the intra-octahedral X-N-X bond angle distributions (Fig. 2 (d-f)), reflecting differences in octahedral flexibility. In  $\text{Sr}_3\text{NSb}$ , the octahedra remains highly symmetric and stable, producing minimal distortion. In contrast,  $\text{Ca}_3\text{NSb}$  exhibits larger deviations, likely due to the smaller mass and size of  $\text{Ca}^{2+}$ , which creates a less constrained bonding environment and increases angular fluctuations.  $\text{Ba}_3\text{NSb}$ , crystallizing in a hexagonal phase, permits anisotropic distortions and enhanced octahedral flexibility, despite the larger ionic radius of  $\text{Ba}^{2+}$ , leading to broader bond-length and angle distributions. These results demonstrate that both ionic size and crystallographic symmetry govern  $\text{NX}_6$  octahedral dynamics.

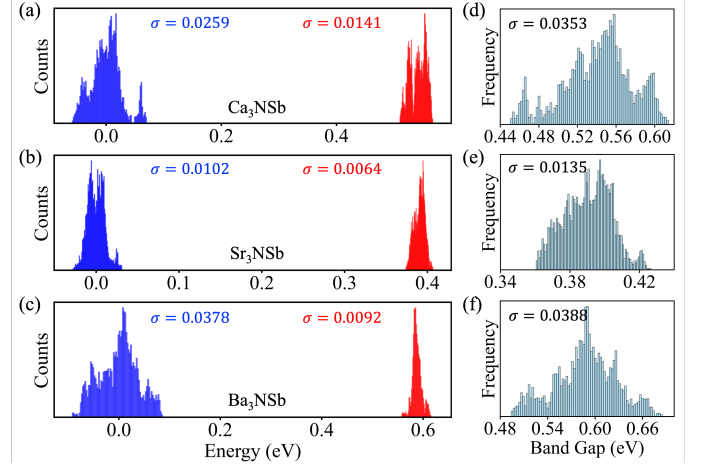


FIG. 3. Statistical distribution of (a-c) VBM (blue) and CBM (red), and (d-f) corresponding band gap distributions, computed using AIMD simulations, for  $\text{Ca}_3\text{NSb}$ ,  $\text{Sr}_3\text{NSb}$ , and  $\text{Ba}_3\text{NSb}$ , respectively. Standard deviations ( $\sigma$ ) of the energy fluctuations are listed.

These structural fluctuations have a direct impact on the electronic structure through electron-phonon interactions. To investigate this effect, we analyze the time-dependent behavior of the VBM and CBM by constructing histograms of their energy levels (Fig.3(a-c)), along with corresponding band gap distributions (Fig.3(d-f)). The data reveal a strong correlation between lattice dynamics and thermal fluctuations in the eigenvalues of the band-edge states. Across all compositions, the VBM exhibits greater temporal fluctuations than the CBM. The standard deviation of the VBM energy follows the trend:  $\text{Ba}_3\text{NSb} > \text{Ca}_3\text{NSb} > \text{Sr}_3\text{NSb}$ , which is consistent with the extent of intra-octahedral X–N bond length and angle fluctuations. In contrast, the CBM standard deviation follows the trend:  $\text{Ca}_3\text{NSb} > \text{Ba}_3\text{NSb} > \text{Sr}_3\text{NSb}$ , indi-

cating a different sensitivity of the conduction band edge to local structural distortions. Among the three systems,  $\text{Sr}_3\text{NSb}$  exhibits the narrowest energy distributions for both VBM and CBM, resulting in the smallest variation in the instantaneous band gap, with a minimum standard deviation of  $\sigma = 0.0135$  eV (Fig. 3(e)). In comparison,  $\text{Ca}_3\text{NSb}$  and  $\text{Ba}_3\text{NSb}$  show larger band gap fluctuations, with standard deviations of approximately 0.0353 eV and 0.0388 eV, respectively. These results demonstrate that cation substitution strongly influences the structural dynamics, which in turn modulate the electronic band-edge energies. The reduced band-edge fluctuations observed in  $\text{Sr}_3\text{NSb}$  suggest weaker electron-phonon coupling and potentially lower nonradiative recombination rates relative to its Ca- and Ba-based counterparts.

#### D. Electron-vibrational interactions

The extent of thermal fluctuations in Kohn-Sham orbital energies indicates the strength of electron-vibration interactions. Inelastic electron-phonon scattering, captured by NA coupling, facilitates energy exchange between electrons and vibrations, enabling nonradiative transitions between electronic states. In contrast, elastic scattering disrupts coherence between the initial and final states during an electronic transition. Although it does not involve direct energy exchange, it significantly influences nonradiative recombination, as transitions can only proceed once quantum coherence between the initial and final states is established. The loss of coherence typically acts to suppress or slow down these transitions, as exemplified by the quantum Zeno effect [51, 52]. Thus, both elastic and inelastic processes play an important role in governing the nonradiative recombination dynamics.

NA coupling, characterizing inelastic electron-vibration scattering, is calculated as:

$$d_{mn} = -i\hbar \langle \varphi_m | \nabla_R | \varphi_n \rangle \cdot \dot{R} = -i\hbar \langle \varphi_m | \frac{\partial}{\partial t} | \varphi_n \rangle$$

where,  $d_{mn}$  is the NA coupling between the initial state  $m$  and final state  $n$ .  $\varphi_m$  and  $\varphi_n$  are their corresponding wavefunctions, and  $R$  denotes the nuclear velocity, determined by the kinetic energy, which is proportional to temperature.  $\langle \varphi_m | \nabla_R | \varphi_n \rangle$  represents the matrix element which quantifies how electronic wavefunctions depend on atomic displacements and requires the wavefunction of VBM and CBM to be confined within the same spatial area. Fig. 1 (d-f) show the charge densities of the VBM and CBM. In all materials, VBM and CBM are predominantly localized on different atomic species, reducing the magnitude of NA coupling. However, it remains non-zero due to minor contributions from other atomic orbitals. Notably, the VBM in  $\text{Sr}_3\text{NSb}$  is comparatively localized than its Ca- and Ba-based counterparts due to reduced Sb-N hybridization, whereas the CBM remains delocalized across the lattice. Table II lists the mean

absolute and root mean square (RMS) value of NA coupling between the VBM and CBM at 300 K. Enhanced octahedral fluctuations and broader energy level distributions in Ba- and Ca-compounds, relative to  $\text{Sr}_3\text{NSb}$ , gradually increase the NA coupling. Higher NA coupling values signify stronger interactions between electron and lattice degrees of freedom, thereby accelerating nonradiative recombination processes.

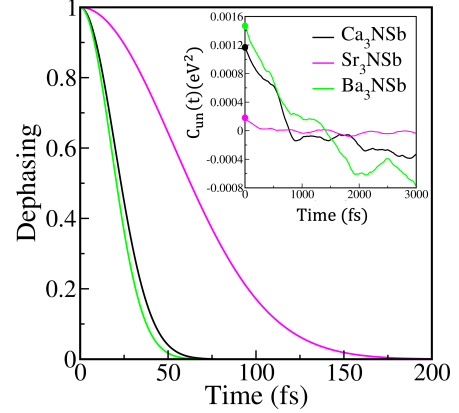


FIG. 4. Pure dephasing functions corresponding to the VBM-CBM transition in  $\text{Ca}_3\text{NSb}$  (black),  $\text{Sr}_3\text{NSb}$  (magenta), and  $\text{Ba}_3\text{NSb}$  (green). The inset displays the unnormalized autocorrelation function (un-ACF), whose initial value (indicated by solid circles) represents the square of the band gap fluctuation. A higher initial un-ACF value typically corresponds to a shorter pure dephasing time.

To characterize elastic electron-phonon interactions, we compute the decoherence times, estimated as pure-dephasing time of the optical response theory. Under the second-order cumulant approximation, the pure-dephasing function is expressed as:

$$D_{ij}(t) = \exp \left( \frac{-1}{\hbar^2} \int_0^t dt' \int_0^{t'} dt'' C_{ij}(t'') \right)$$

where  $C_{ij}(t) = \langle \delta E_{ij}(t) \delta E_{ij}(0) \rangle$  is the unnormalized autocorrelation function of the phonon-induced band gap fluctuation.  $E_{ij}(t) = E_{ij}(t) - \langle E_{ij} \rangle$  represents the fluctuation of the energy gap between states  $i$  and  $j$ , and  $\langle E_{ij} \rangle$  denotes the ensemble-averaged band gap. The pure-dephasing (or decoherence) time is extracted by fitting  $D_{ij}(t)$  (Fig. 4) to a Gaussian decay function of the form:  $f(t) = \exp(-0.5(\frac{t}{\tau})^2)$ , with the corresponding values summarized in Table II. The initial value of the un-ACF,  $C_{ij}(0)$ , represents the square of band gap fluctuation. The calculated band gap variances (in Fig. 3 (d-f)) corroborate the un-ACF initial values, which decrease in the sequence  $\text{Sr}_3\text{NSb} < \text{Ca}_3\text{NSb} < \text{Ba}_3\text{NSb}$ . Greater initial value of un-ACF and more asymmetric ACF favor faster dephasing. The pure dephasing times decrease in the opposite order,  $\text{Ba}_3\text{NSb} < \text{Ca}_3\text{NSb} < \text{Sr}_3\text{NSb}$ , as expected. The suppression of decoherence/pure dephasing in the Ca- or Ba-containing systems is attributed to



TABLE II. Canonically averaged scaled band gaps (in eV), with original band gaps included in parenthesis, along with the averaged absolute nonadiabatic (NA) coupling, root mean square (RMS) value of NA coupling, pure-dephasing time, and nonradiative electron-hole recombination lifetime for the VBM-CBM transition in  $\text{Ca}_3\text{NSb}$ ,  $\text{Sr}_3\text{NSb}$ , and  $\text{Ba}_3\text{NSb}$ .

$\text{X}_3\text{NSb}$	Gap (eV)	NA coupling (meV)	RMS NA coupling (meV)	Dephasing (fs)	Recombination (ns)
$\text{Ca}_3\text{NSb}$	1.33 (0.54)	0.57	1.02	20.3	1.36
$\text{Sr}_3\text{NSb}$	1.14 (0.38)	0.26	0.50	52.8	3.48
$\text{Ba}_3\text{NSb}$	1.57 (0.59)	0.67	1.20	17.4	2.27

enhanced electronic energy level fluctuations in comparison to  $\text{Sr}_3\text{NSb}$ . The pure-dephasing times of  $\text{X}_3\text{NSb}$  compounds (17-53 fs) are much shorter than the electron-hole recombination time. Therefore, it is necessary to include decoherence into the NAMD simulations.

### E. Nonradiative electron-hole recombination

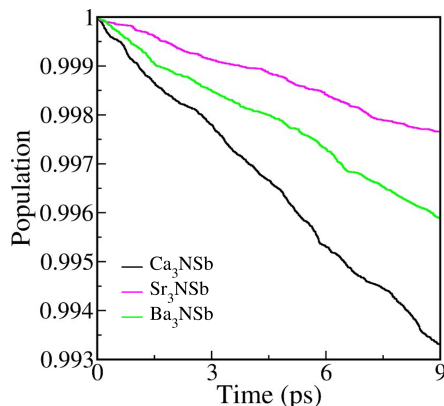


FIG. 5. Nonradiative electron-hole recombination dynamics associated with the VBM-CBM transition in  $\text{Ca}_3\text{NSb}$  (black),  $\text{Sr}_3\text{NSb}$  (magenta), and  $\text{Ba}_3\text{NSb}$  (green).

Fig. 5 depicts the time evolution of first-excited state populations during nonradiative electron-hole recombination in  $\text{X}_3\text{NSb}$  antiperovskites. Since PBE systematically underestimates the band gap, the gaps are rescaled to their corresponding  $G_0W_0@HSE06+SOC$  values (listed in Table II), which reproduce experimental values for  $\text{Sr}_3\text{NSb}$  [17]. Given that intraband relaxation in semiconductors typically occurs on sub-picosecond timescales, we assume that the electron and hole have already relaxed to the CBM and VBM, respectively. Recombination time constants are extracted by fitting the population decay to an exponential function,  $P(t) = \exp(-t/\tau)$ , and the resulting lifetimes are summarized in Table II. NAMD simulations reveal the following trend in recombination lifetimes:  $\text{Sr}_3\text{NSb}$  (3.48 ns) >  $\text{Ba}_3\text{NSb}$  (2.27 ns) >  $\text{Ca}_3\text{NSb}$  (1.36 ns). These lifetimes are mainly governed by the interplay of three key parameters: (a) the band gap, (b) the strength of NA coupling, and (c) the pure-dephasing time. In general, larger band gaps, weaker NA coupling, and shorter dephasing

times are expected to suppress nonradiative recombination and prolong carrier lifetimes. The interdependence of these parameters makes their collective influence on carrier dynamics complex and non-intuitive.  $\text{Sr}_3\text{NSb}$  exhibits the longest lifetime despite having a smaller band gap and longer dephasing time compared to other compounds. This behavior is primarily attributed to its significantly weaker NA coupling (0.26 meV), which dominates the recombination dynamics. The comparison between  $\text{Ba}_3\text{NSb}$  and  $\text{Ca}_3\text{NSb}$  further underscores the competing roles of these factors. Although both compounds exhibit comparable NAC values (0.67 meV for Ba and 0.57 meV for Ca),  $\text{Ba}_3\text{NSb}$  features a larger band gap of around 1.57 eV and a shorter pure-dephasing time, resulting in a longer recombination lifetime than  $\text{Ca}_3\text{NSb}$ . Overall, slower nonradiative recombination mitigates energy losses and increases the performance of solar cells.

## IV. CONCLUSION

Using a combination of NAMD and TDDFT, we investigated the influence of X-site cation substitution on nonradiative electron-hole recombination dynamics in  $\text{X}_3\text{NSb}$  ( $\text{X} = \text{Ca}, \text{Sr}, \text{and Ba}$ ) antiperovskite nitrides. While  $\text{Ca}_3\text{NSb}$  and  $\text{Sr}_3\text{NSb}$  adopt a cubic perovskite structure in their ground state,  $\text{Ba}_3\text{NSb}$  stabilizes in a distorted hexagonal phase, resulting in markedly different structural and recombination behaviors. In the cubic phases, increasing cation size narrows the band gap through a downward shift of the X  $d$  orbitals, thereby lowering the CBM. In contrast, the lattice distortion in  $\text{Ba}_3\text{NSb}$  leads to an increase in the band gap, consistent with the trends observed in LHPs. Further, band structure calculations reveal that all three compounds are direct band gap semiconductor with band edges located at the  $\Gamma$  point.

AIMD simulations at 300 K reveal the X-site cation strongly impacts the amplitude of atomic motions and octahedral dynamics. In the cubic phases, larger X-site cations suppress octahedral and band edge fluctuations, resulting in weaker NA coupling. While, the hexagonal phase of  $\text{Ba}_3\text{NSb}$  exhibits enhanced structural fluctuations and stronger NA coupling. Pure-dephasing times, governed by band gap fluctuations, follow  $\text{Sr}_3\text{NSb}$  (52.8 fs) >  $\text{Ca}_3\text{NSb}$  (20.3 fs) >  $\text{Ba}_3\text{NSb}$  (17.4 fs). The interplay between the band gap, NA coupling and dephasing time determine recombination lifetimes. Weak NA cou-

pling suppresses recombination, whereas small band gaps and long dephasing times accelerate it.  $\text{Sr}_3\text{NSb}$  exhibits the longest recombination lifetime due to its weakest NA coupling among studied antiperovskites. While faster dephasing and larger band gap in  $\text{Ba}_3\text{NSb}$  leads to longer recombination lifetime than  $\text{Ca}_3\text{NSb}$ . Overall, both X-site cation chemistry and structural symmetry critically shape the structural, electronic, and recombination dynamics of  $\text{X}_3\text{NSb}$  antiperovskites. These findings provide design principles for engineering long-lived excited states by suppressing nonradiative recombination.

## V. ACKNOWLEDGMENT

S.M. acknowledge IIT Delhi for the senior research fellowship. S.B. acknowledge financial support from SERB under a core research grant [Grant no. CRG/2019/000647] to set up his High Performance Computing (HPC) facility “Veena” at IIT Delhi for computational resources.

- 
- [1] M. A. Green, A. Ho-Baillie, and H. J. Snaith, The emergence of perovskite solar cells, *Nat. Photonics* **8**, 506 (2014).
  - [2] W.-J. Yin, J.-H. Yang, J. Kang, Y. Yan, and S.-H. Wei, Halide perovskite materials for solar cells: a theoretical review, *J. Mater. Chem. A* **3**, 8926 (2015).
  - [3] J. Y. Kim, J.-W. Lee, H. S. Jung, H. Shin, and N.-G. Park, High-efficiency perovskite solar cells, *Chem. Rev.* **120**, 7867 (2020).
  - [4] X. Yu, H. N. Tsao, Z. Zhang, and P. Gao, Miscellaneous and perspicacious: Hybrid halide perovskite materials based photodetectors and sensors, *Adv. Opt. Mater.* **8**, 2001095 (2020).
  - [5] National renewable energy laboratory (nrel). best research-cell efficiency chart., <https://www.nrel.gov/pv/cell-efficiency.html>, (accessed: January 26, 2021).
  - [6] G. Schileo and G. Grancini, Lead or no lead? availability, toxicity, sustainability and environmental impact of lead-free perovskite solar cells, *J. Mater. Chem. C* **9**, 67 (2021).
  - [7] M.-G. Ju, M. Chen, Y. Zhou, J. Dai, L. Ma, N. P. Padture, and X. C. Zeng, Toward eco-friendly and stable perovskite materials for photovoltaics, *Joule* **2**, 1231 (2018).
  - [8] E. Chi, W. Kim, N. Hur, and D. Jung, New mg-based antiperovskites  $\text{PnNMg}_3$  ( $\text{Pn} = \text{As}, \text{Sb}$ ), *Solid State Commun.* **121**, 309 (2002).
  - [9] B. Beznosikov, Predicted nitrides with an antiperovskite structure, *J. Struct. Chem.* **44**, 885 (2003).
  - [10] K. N. Heinselman, S. Lany, J. D. Perkins, K. R. Talley, and A. Zakutayev, Thin film synthesis of semiconductors in the  $\text{Mg} - \text{Sb} - \text{N}$  materials system, *Chem. Mater.* **31**, 8717 (2019).
  - [11] Y. Mochizuki, H.-J. Sung, A. Takahashi, Y. Kumagai, and F. Oba, Theoretical exploration of mixed-anion antiperovskite semiconductors  $\text{M}_3\text{XN}$  ( $\text{M} = \text{Mg}, \text{Ca}, \text{Sr}, \text{Ba}$ ;  $\text{X} = \text{P}, \text{As}, \text{Sb}, \text{Bi}$ ), *Phys. Rev. Mater.* **4**, 044601 (2020).
  - [12] H. Zhong, C. Feng, H. Wang, D. Han, G. Yu, W. Xiong, Y. Li, M. Yang, G. Tang, and S. Yuan, Structure–composition–property relationships in antiperovskite nitrides: Guiding a rational alloy design, *ACS Appl. Mater. Interfaces* **13**, 48516 (2021).
  - [13] Y. Wang, H. Zhang, J. Zhu, X. Lü, S. Li, R. Zou, and Y. Zhao, Antiperovskites with exceptional functionalities, *Adv. Mater.* **32**, 1905007 (2020).
  - [14] J. Dai, M.-G. Ju, L. Ma, and X. C. Zeng,  $\text{Bi}(\text{Sb})\text{NCa}_3$ : Expansion of perovskite photovoltaics into all-inorganic anti-perovskite materials, *J. Phys. Chem. C* **123**, 6363 (2019).
  - [15] Y. Kang, Antiperovskite  $\text{Sr}_3\text{MN}$  and  $\text{Ba}_3\text{MN}$  ( $\text{M} = \text{Sb}$  or  $\text{Bi}$ ) as promising photovoltaic absorbers for thin-film solar cells: A first-principles study, *J. Am. Ceram. Soc.* **105**, 5807 (2022).
  - [16] F. Gäbler, M. Kirchner, W. Schnelle, U. Schwarz, M. Schmitt, H. Rosner, and R. Niewa,  $(\text{Sr}_3\text{N})\text{E}$  and  $(\text{Ba}_3\text{N})\text{E}$  ( $\text{E} = \text{Sb}, \text{Bi}$ ): Synthesis, crystal structures, and physical properties, *Z Anorg Allg Chem* **630**, 2292 (2004).
  - [17] S. Monga, M. Jain, C. Draxl, and S. Bhattacharya, Theoretical insights into inorganic antiperovskite nitrides ( $\text{X}_3\text{NA}$ :  $\text{X} = \text{Mg}, \text{Ca}, \text{Sr}, \text{Ba}$ ;  $\text{A} = \text{As}, \text{Sb}$ ): An emerging class of materials for photovoltaics, *Phys. Rev. Mater.* **8**, 105403 (2024).
  - [18] K.-P. Wang, X. Dong, J.-Z. Yuan, B. Wen, J. He, C.-J. Tong, and O. V. Prezhdo, Self-Passivation at the  $\text{SnO}_2/\text{Perovskite}$  Interface, *ACS Energy Lett.* **10**, 1466 (2025).
  - [19] K.-P. Wang, Z.-W. Wu, K.-F. Wang, H.-T. Xu, J. He, B. Wen, C.-J. Tong, L.-M. Liu, and O. V. Prezhdo, Detrimental Defect Cooperativity at  $\text{TiO}_2/\text{CH}_3\text{NH}_3\text{PbI}_3$  Interface: Decreased Stability, Enhanced Ion Diffusion, and Reduced Charge Lifetime and Transport, *ACS Energy Lett.* **9**, 5888 (2024).
  - [20] J. Chen, M. E. Messing, K. Zheng, and T. Pullerits, Cation-dependent hot carrier cooling in halide perovskite nanocrystals, *J. Am. Chem. Soc.* **141**, 3532 (2019).
  - [21] C. de Weerd, L. Gomez, A. Capretti, D. M. Lebrun, E. Matsubara, J. Lin, M. Ashida, F. C. Spoor, L. D. Siebbeles, A. J. Houtepen, *et al.*, Efficient carrier multiplication in  $\text{CsPbI}_3$  perovskite nanocrystals, *Nat. Commun.* **9**, 4199 (2018).
  - [22] P. K. Nayak and D. Ghosh, Optimizing excited charge dynamics in layered halide perovskites through compositional engineering, *Nano Lett.* (2025).
  - [23] L. Qiao, M. Guo, and R. Long, Unveiling the dual role of humidity: The interplay with defects manipulating the charge carrier lifetime in metal halide perovskites, *J. Phys. Chem. Lett.* **15**, 1546 (2024).
  - [24] R. Shi, Q. Fang, A. S. Vasenko, R. Long, W.-H. Fang, and O. V. Prezhdo, Structural disorder in higher-temperature phases increases charge carrier lifetimes in metal halide perovskites, *J. Am. Chem. Soc.* **144**, 19137 (2022).

- [25] X. Ma, X. Tian, E. Stippell, O. V. Prezhdo, R. Long, and W.-H. Fang, Self-passivation of halide interstitial defects by organic cations in hybrid lead-halide perovskites: Ab initio quantum dynamics, *J. Am. Chem. Soc.* **146**, 29255 (2024).
- [26] W. Li, Y. She, A. S. Vasenko, and O. V. Prezhdo, Ab initio nonadiabatic molecular dynamics of charge carriers in metal halide perovskites, *Nanoscale* **13**, 10239 (2021).
- [27] W. Li, J. Tang, D. Casanova, and O. V. Prezhdo, Time-domain ab initio analysis rationalizes the unusual temperature dependence of charge carrier relaxation in lead halide perovskite, *ACS Energy Lett.* **3**, 2713 (2018).
- [28] J. Wang and R. Long, Nuclear quantum effects accelerate charge recombination but boost the stability of inorganic perovskites in mild humidity, *Nano Lett.* **24**, 3476 (2024).
- [29] S. Panigrahi, M. Sk, S. Jana, S. Ghosh, J. Deuermeier, R. Martins, and E. Fortunato, Tailoring the interface in high performance planar perovskite solar cell by ZnOS thin film, *ACS Appl. Energy Mater.* **5**, 5680 (2022).
- [30] B. Du, Q. Wei, Y. Cai, T. Liu, B. Wu, Y. Li, Y. Chen, Y. Xia, G. Xing, and W. Huang, Crystal face dependent charge carrier extraction in  $\text{TiO}_2$ /perovskite heterojunctions, *Nano Energy* **67**, 104227 (2020).
- [31] E. Runge and E. K. Gross, Density-functional theory for time-dependent systems, *Phys. Rev. Lett.* **52**, 997 (1984).
- [32] C. F. Craig, W. R. Duncan, and O. V. Prezhdo, Trajectory Surface Hopping in the Time-Dependent Kohn-Sham Approach for Electron-Nuclear Dynamics, *Phys. Rev. Lett.* **95**, 163001 (2005).
- [33] H. M. Jaeger, S. Fischer, and O. V. Prezhdo, Decoherence-induced surface hopping, *J. Chem. Phys.* **137** (2012).
- [34] A. V. Akimov and O. V. Prezhdo, The pyxaid program for non-adiabatic molecular dynamics in condensed matter systems, *J. Chem. Theory Comput.* **9**, 4959 (2013).
- [35] A. V. Akimov and O. V. Prezhdo, Advanced capabilities of the pyxaid program: integration schemes, decoherence effects, multiexcitonic states, and field-matter interaction, *J. Chem. Theory Comput.* **10**, 789 (2014).
- [36] P. Hamm, Principles of nonlinear optical spectroscopy: A practical approach or: Mukamel for dummies, *University of Zurich* **41**, 77 (2005).
- [37] P. Hohenberg and W. Kohn, Inhomogeneous electron gas, *Phys. Rev.* **136**, B864 (1964).
- [38] W. Kohn and L. J. Sham, Self-consistent equations including exchange and correlation effects, *Phys. Rev.* **140**, A1133 (1965).
- [39] G. Kresse and J. Furthmüller, Efficiency of ab-initio total energy calculations for metals and semiconductors using a plane-wave basis set, *Comput. Mater. Sci.* **6**, 15 (1996).
- [40] G. Kresse and D. Joubert, From ultrasoft pseudopotentials to the projector augmented-wave method, *Phys. Rev. B* **59**, 1758 (1999).
- [41] P. E. Blöchl, Projector augmented-wave method, *Phys. Rev. B* **50**, 17953 (1994).
- [42] J. P. Perdew, K. Burke, and M. Ernzerhof, Generalized gradient approximation made simple, *Phys. Rev. Lett.* **77**, 3865 (1996).
- [43] D. Stoiber and R. Niewa, Perovskite distortion inverted: Crystal structures of  $(\text{A}_3\text{N})\text{As}$  ( $\text{A} = \text{Mg}, \text{Ca}, \text{Sr}, \text{Ba}$ ), *Z Anorg Allg Chem* **645**, 329 (2019).
- [44] A. V. Krukau, O. A. Vydrov, A. F. Izmaylov, and G. E. Scuseria, Influence of the exchange screening parameter on the performance of screened hybrid functionals, *J. Chem. Phys.* **125**, 224106 (2006).
- [45] P. Giannozzi, S. Baroni, N. Bonini, M. Calandra, R. Car, C. Cavazzoni, D. Ceresoli, G. L. Chiarotti, M. Cococcioni, I. Dabo, *et al.*, QUANTUM ESPRESSO: a modular and open-source software project for quantum simulations of materials, *J. Phys.: Condens. Matter* **21**, 395502 (2009).
- [46] B. Wang, W. Chu, Y. Wu, W. A. Saidi, and O. V. Prezhdo, Sub-bandgap charge harvesting and energy up-conversion in metal halide perovskites: ab initio quantum dynamics, *npj Comput. Mater.* **11**, 11 (2025).
- [47] B. Yang, B. Cai, J. Xia, Y. Liu, Y. Ma, J. Zhang, L. Liu, K. Cao, W. Shen, S. Chen, *et al.*, Reducing nonradiative recombination in halide perovskites through appropriate band gaps and heavy atomic masses, *J. Phys. Chem. Lett.* **16**, 1253 (2025).
- [48] R. Prasanna, A. Gold-Parker, T. Leijtens, B. Conings, A. Babayigit, H.-G. Boyen, M. F. Toney, and M. D. McGehee, Band gap tuning via lattice contraction and octahedral tilting in perovskite materials for photovoltaics, *J. Am. Chem. Soc.* **139**, 11117 (2017).
- [49] J. L. Knutson, J. D. Martin, and D. B. Mitzi, Tuning the band gap in hybrid tin iodide perovskite semiconductors using structural templating, *Inorg. Chem.* **44**, 4699 (2005).
- [50] L. Kong, G. Liu, J. Gong, Q. Hu, R. D. Schaller, P. Dera, D. Zhang, Z. Liu, W. Yang, K. Zhu, *et al.*, Simultaneous band-gap narrowing and carrier-lifetime prolongation of organic-inorganic trihalide perovskites, *Proc. Natl. Acad. Sci. U.S.A.* **113**, 8910 (2016).
- [51] O. V. Prezhdo, Quantum anti-zeno acceleration of a chemical reaction, *Phys. Rev. Lett.* **85**, 4413 (2000).
- [52] S. V. Kilina, A. J. Neukirch, B. F. Habenicht, D. S. Kilin, and O. V. Prezhdo, Quantum zeno effect rationalizes the phonon bottleneck in semiconductor quantum dots, *Phys. Rev. Lett.* **110**, 180404 (2013).